Journal of Power Sources 214 (2012) 159–165

Contents lists available at SciVerse ScienceDirect

Journal of Power Sources

journal homepage: www.elsevier.com/locate/jpowsour

Electrochemical and structural analysis of Al-doped ZnO nanorod arrays in dye-sensitized solar cells

Runbang Tao, Takahiro Tomita, Raymond Albert Wong, Keiko Waki*

Interdisciplinary Graduate School of Science and Engineering, Tokyo Institute of Technology, Department of Energy Sciences, 4259 Nagatsuta-cho, Midori-ku, Yokohama-shi 226-8502, Japan

HIGHLIGHTS

- Al-doped ZnO nanorod arrays for photoanode for dye-sensitized solar cells.
- The open-circuit voltage increased significantly with the addition of Al, up from 0.636 V to 0.732 V
- Diameter of nanorods changed with the addition of Al.
- Appropriate increase in nanorod diameter is considered favorable for performance.

GRAPHICAL ABSTRACT

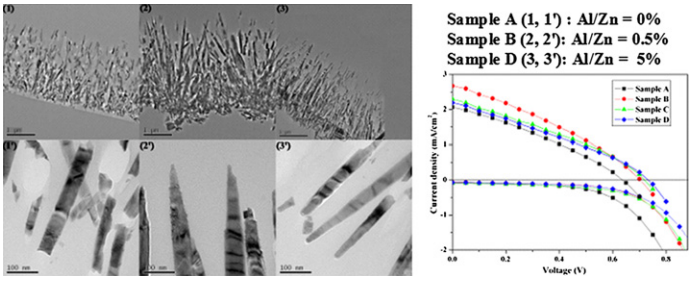

ARTICLE INFO

Article history:
Received 12 December 2011
Received in revised form
10 March 2012
Accepted 25 April 2012
Available online 3 May 2012

Keywords:
Al-doped ZnO nanorod arrays
Dye-sensitized solar cells
Morphological
Structural changes
Increase in open-circuit voltage

ABSTRACT

Al-doped ZnO nanorod arrays with the Al contents in the region of 0–5% were prepared and evaluated as photoanodes for dye-sensitized solar cells (DSSCs). It was found that Al-doping has changed not only electrical properties but also the morphology and structure of the ZnO nanorods. The open-circuit voltage increased significantly with the addition of Al, up from 0.636 V to 0.732 V, due to the increase in electron recombination resistance at the ZnO nanorod array electrode/electrolyte interfaces resulting in the reduction in dark current. The diameter of the ZnO nanorods also changes with the addition of Al. Our results indicate that an appropriate increase in the diameter of the nanorods is favorable due to the reduction in electron transport resistance, which further speeds up electron transport in the ZnO nanorod arrays leading to the increase of short-circuit current. Of the samples analyzed, the DSSC containing Al-doped ZnO nanorod arrays of 0.5% exhibits the highest efficiency due to its increased open-circuit voltage and short-circuit current.

1. Introduction

Dye-sensitized solar cells (DSSCs) have recently attracted considerable attention due to their promising potential for high efficiency and low production cost [1,2]. Conventional photoanode electrodes for DSSCs are based on TiO_2 [1], ZnO [3], or Nb_2O_5 [4] nanoparticles. The resistance in the nanoparticle–nanoparticle interface encourages multiple trapping/detrapping events which results in slow electron transport rates and greater recombination [5]. In order to achieve further improvements in electron transport, many studies have focused on DSSC photoanodes containing one-dimensional nanostructures such as nanotubes [6–8], nanofibers [9], and nanorods [10,11]. Among these studies, ZnO nanorod array electrodes have attracted significant attention due to their favorable properties such as electron mobility and ease of fabrication. However, when compared with traditional TiO_2 electrodes, ZnO nanorod arrays still suffer because of their insufficient surface area for dye adsorption [11]. Due to this reason, significant research focuses on increasing the surface area for dye absorption [12–14]. Instead of increasing the surface area for dye absorption, Al-doping

* Corresponding author. Tel./fax: +81 45 924 5614.
E-mail addresses: wen@es.titech.ac.jp, waki.k.aa@titech.ac.jp (K. Waki).

0378-7753/$ – see front matter © 2012 Elsevier B.V. All rights reserved.
doi:10.1016/j.jpowsour.2012.04.071

offers performance improvements based on the preexisting nanorod array structure. Another motivating factor of this report is that there has been no thorough report on the electrochemical details of Al-doped ZnO nanorod arrays used as photoanode materials in DSSCs. The structural and electrochemical properties, induced by Al-doping, are studied in detail and found to be beneficial in improving the performance for ZnO nanorod based DSSCs.

2. Experimental section

2.1. Synthesis of Al-doped ZnO nanorod arrays

The vertically aligned Al-doped ZnO nanorod arrays were synthesized via a two-step chemical bath deposition (CBD) procedure. First, the ZnO nanoparticle-based seed layer on the ITO glass substrate (5 Ω sq^{-1}, Geomatec) was prepared with a sol-gel method. 0.6 M zinc acetate dihydrate ($Zn(CH_3COO)_2 \cdot 2H_2O$, >99%, Wako), 0.6 M monoethanolamine (C_2H_7NO, >99%, Wako) and 2-methoxyethanol ($C_3H_8O_2$, >99%, Wako) were used, respectively. The resultant solution was stirred at 70 °C for 1 h until a clear and homogeneous solution was formed. The solution was then spin-coated onto multiple ITO glass plates (exposure area of 1 cm^2) for 30 s at 3000 rpm. The coated ITO glass substrates were subsequently pre-heated at 250 °C for 10 min. The pre-heating treatment is required to remove that undesired solvent and organic residuals. The spin coating and heating procedures were repeated 3 times in order to form a dense layer. Afterward, the coated seed layer was annealed at 400 °C for 1 h as a post-heating treatment. The Al-doped ZnO nanorod arrays were subsequently obtained by immersing the inverted seeded substrate in a chemical growth solution containing 0.05 M zinc nitrate hexahydrate ($Zn(NO_3)_2 \cdot 6H_2O$, >99%, Wako), 0.75 M aqueous ammonia ($NH_3 \cdot H_2O$, 10 wt.%, Wako), and low concentrations of aluminum nitrate nonahydrate ($Al(NO_3)_3 \cdot 9H_2O$, >99%, Wako) in a sealed polypropylene (PP) bottle. The PP bottle was inserted into an air oven and heated to 100 °C without stirring for 2 h. The concentrations of Al in the growth solution are referred as Al/Zn molar ratios, and are 0, 0.5%, 2.5%, and 5.0%, respectively. For convenience, the corresponding ZnO nanorod array electrodes are designated as sample A, sample B, sample C, and sample D, respectively.

2.2. DSSC cell assembly

The dye adsorption was carried out by immersing the electrodes in a 0.5 mM ethanolic solution of Di-tetrabutylammonium cis-bis(isothiocyanato)bis(2,2′-bipyridyl-4,4′-dicarboxylato)ruthenium (II) (N719, Solaronix) for 4 h. The mirror-like Pt coated ITO glasses were fabricated as counter electrodes, by RF-magnetron sputtering, using a pure platinum target in ambient Ar gas, with an RF power of 30 W for 3 min at room temperature of 25 °C. The sensitized electrode was layered with the platinum-coated ITO counter electrode, sandwiched by a 50 μm-thick hot-melt spacer (Mitsui Chem). This study employed the use of standard liquid electrolyte, which consists of 0.1 M LiI (Wako), 50 mM I_2 (Wako), 0.6 M 1, 2-dimethyl-3-propylimidazolium iodide (Shikoku Chem), and 0.5 M 4-tert-butyl pyridine (Tokyokasei Kogyo) in acetonitrile (Dojindo). The active area of the device was held fixed at 1 cm^2 by the use of a metal mask.

2.3. Characterization

The crystal structures of the un-doped and Al-doped ZnO nanorod arrays were investigated by using an *X*-ray diffraction spectrometer (XRD, Rigaku RINT-2000) with the Cu radiation source at 40 kV and 30 mA, from 25° to 70° in 2θ. The morphology and structure of the ZnO nanorod arrays were observed using scanning electron microscopes (SEM, Keyence VE-7800 and JEOL JSM-6610LA) and a field emission transmission electron microscope (FE-TEM, JEOL JEM-2010F). The elemental composition was analyzed by an energy dispersive *X*-ray (EDX) analysis attachment (EDAX, Genesis) on the FE-TEM. The evaluation of the dye loading was examined by following procedures. The dyes were desorbed from the sensitized electrodes by immersing the electrodes in 0.1 M KOH ethanol–water (volume ratio = 1:1) solution. The solutions were then studied using a UV–visible spectrophotometer (JASCO V-570). The solar cell photovoltaic properties of the assembled cells were evaluated by recording the *I–V* characteristics under dark and light illumination conditions (light intensity: 200 mW cm^{-2}, illuminance: 120,000 Lux). A high power Xenon lamp (Yamada kogaku kogyo) was used as the light source. For the further investigation of the electron transport properties, the impedance measurements were performed using a modular potentiostat (Autolab PSTA30) with a frequency response analyzer under open-circuit voltage (V_{oc}) conditions, with constant light illumination (light intensity: 200 mW cm^{-2}, illuminance: 120,000 Lux). The examined frequency range was from 10^{-1} Hz–10^5 Hz with an AC amplitude of 10 mV.

3. Results and discussion

The top-perspective of the ZnO nanorod arrays with their respective Al contents are shown in the SEM images in Fig. 1 and the FE-TEM images of sample A, B, D are shown in Fig. 2. The FE-TEM images in Fig. 2 indicate that the base portion of the ZnO nanorods is thicker, while the top portion tends to be thinner. This type of ZnO nanorod structure with nanopencil-like morphology has been previously reported [15]. The FE-TEM images show that the relative size of the ZnO nanorods varies with the Al-doping concentration and that sample B contains the largest diameter and length. The diameter and length clearly increases between 0% doping and 0.5% doping. However, this trend does not continue, as there is a drop in diameter and length between 0.5% and 5% Al-doping. Therefore, it is reasonable to suggest that there is some correlation between the structural variation of the ZnO nanorods and the Al-doping concentration. For the ease of comparison, the variation in the average diameter and length of the ZnO nanorod arrays observed by FE-TEM is shown in Fig. 3. The detection of Al content in the ZnO nanorods was done via EDX analysis, which was conducted concurrently during FE-TEM operation. Based on the EDX results, the calculated Al contents measured for the upper portion of ZnO nanorods are about 0 at. %, 0.54 at. % and 4.7 at. %, respectively. This is consistent with the corresponding Al-doping concentration in the ZnO nanorod growth solution. XRD analysis was used to investigate the crystal structures of the ZnO nanorod array thin films. The XRD patterns of the ZnO nanorod arrays on the ITO glass substrate can be seen in Fig. 4. It can be clearly seen that all of the samples exhibit a sharp and strong peak at about 34–35°, which corresponds to the (002) direction of ZnO with wurtzite structure (JCPDS card number 36–1451). Other than the strong peak at 34–35°, no additional characteristic peaks of Al or Al_2O_3 were detected. Therefore, it can be concluded with certainty that the Al-doped ZnO nanorod arrays tend to grow along the *c*-axis direction, which is perpendicular to the substrate interface. This indicates that our ZnO nanorod arrays contain the desired perpendicular crystalline structure. The conducted SEM and FE-TEM analysis also supports this finding. Fig. 5 displays the variation of the full width at half maximum (FWHM) and the *c*-axis lattice constant in the (002) orientation of the ZnO nanorod arrays as a function of the Al content derived from the XRD patterns. In this study, the FWHM values were calibrated for instrumental broadening with reference to the silicon diffraction line. Fig. 5 indicates that the FWHM and the *c*-axis lattice constant decreases

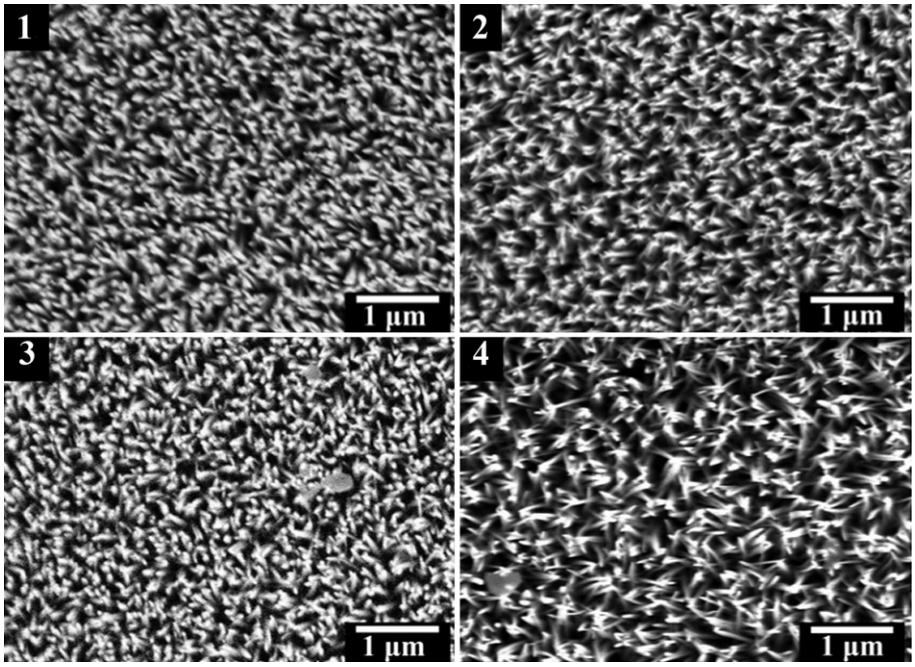

Fig. 1. Top-view SEM images of the Al-doped ZnO nanorod arrays: (1) Sample A, (2) Sample B, (3) sample C and (4) Sample D.

at first and then subsequently increases with higher levels of Al content. The two parameters reach the minimum value in sample B. It is known that the FWHM and the *c*-axis lattice constant can be applied to characterize and evaluate crystal quality. The FWHM value is inversely proportional to the crystal size according to the Debye–Scherer formula. Therefore, the variation of the FWHM is in accordance with the variation in the diameter and length of the ZnO nanorods as a function of the Al content, which is also in agreement with the FE-TEM results. In general terms, the impurity mechanism suggests that the introduction of impurities and defects can result in the formation of grain boundaries which diminishes the grain size [16,17]. On the other hand, for the hexagonal wurtzite phase with highly *c*-axis preferred orientation, the in-plane stress can be attributed to a compressive stress and the absolute value of the stress is proportional to the value of the *c*-axis lattice constant based on the biaxial strain model [18,19]. For Al-doping, Al^{3+} is

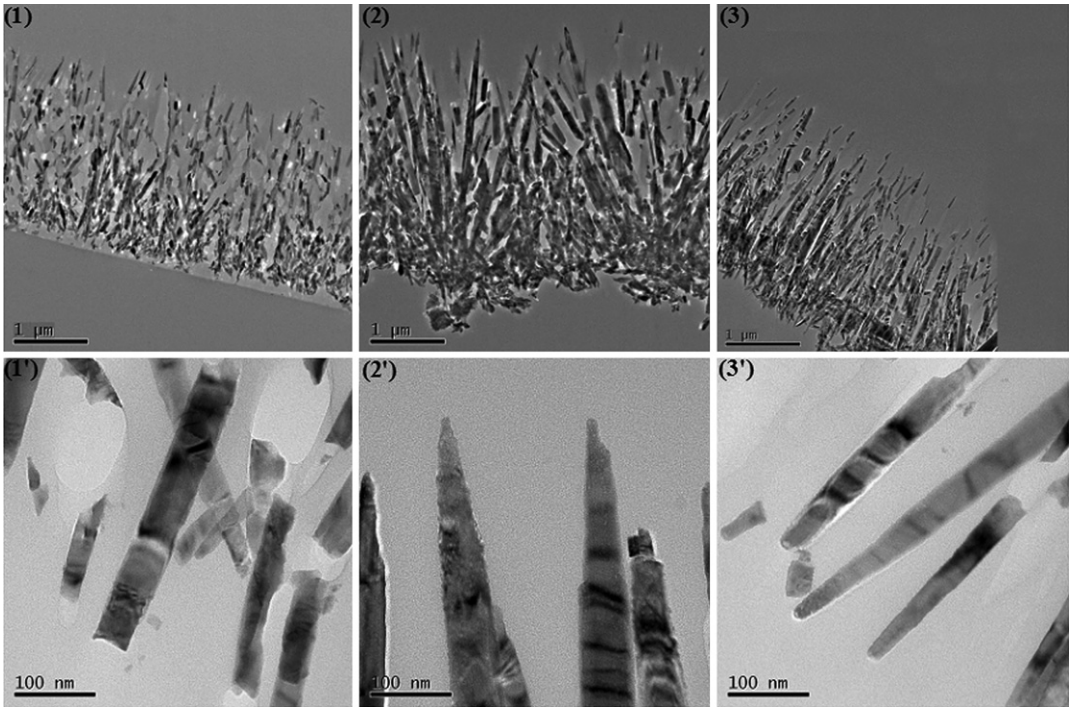

Fig. 2. FE-TEM images of the Al-doped ZnO nanorod arrays: (1, 1′) Sample A, (2, 2′) Sample B and (3, 3′) Sample D.

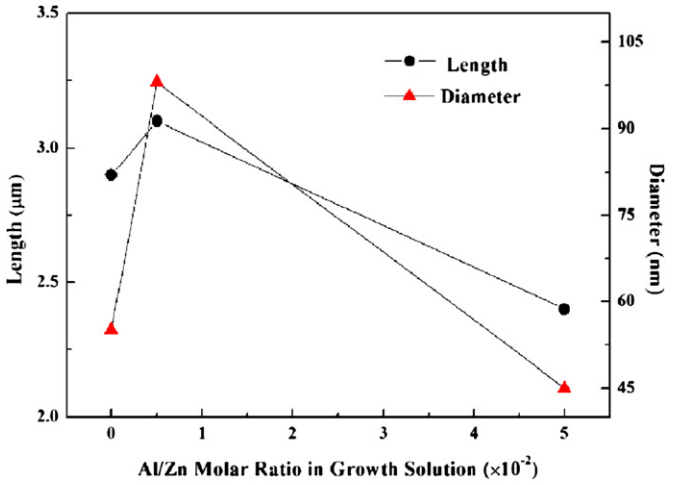

Fig. 3. The variation in the average length and diameter of the ZnO nanorod arrays as a function of the Al content derived from FE-TEM images.

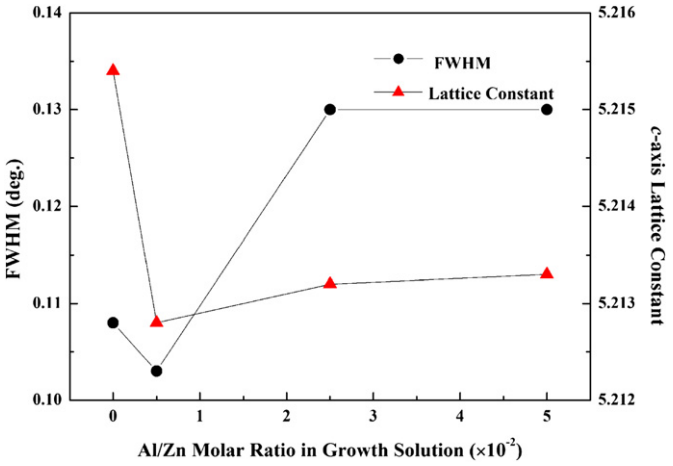

Fig. 5. The variation of FWHM and *c*-axis lattice constant in the (002) orientation of the ZnO nanorod arrays as a function of the Al content derived from XRD patterns.

introduced into ZnO and thus, Al^{3+} is allowed to replace Zn^{2+}. The Al-doping leads to a decrease in the *c*-axis lattice constant which results in the release of the residually compressive stress, because the ion radius of Al^{3+} (~0.053 nm) is smaller than Zn^{2+} (~0.074 nm) [20]. However, with higher values of Al-doping concentration, the superfluous Al^{3+} could be located at interstitial sites, leading to the increment of the *c*-axis lattice constant and thus increase compressive stress. Lu et al. proposed that Al-doping releases compressive stress, leading an increase of the crystal grain size in ZnO particle thin films [19]. Our results confirm that the residual stress relieving effects attributed by Al-doping, contribute to the crystal-growth rates and this behavior can been seen in the diameter and length increase for the 0.5% Al-doped ZnO nanorod arrays. However, the range of Al-doping concentration values that correspond to the relieving of residual stress is substantially lower in our Al-doped ZnO nanorods study than in ZnO particle thin films. This is the first time the details of the diameter and length increase of Al-doped ZnO nanorod arrays have been reported. In order to investigate the trend of the surface area changes, dye loading was further evaluated by UV–visible spectroscopy measurements. As shown in Fig. 6, there exists a strong peak at around 510 nm, induced by N719 dye molecules. Therefore, the absorbance is proportional to the dye loading amount. The amount of dye loading varies with the Al content, due to the surface area difference induced by Al-doping. The dye loading amount of sample B is relatively small in comparison to the other samples. A plausible explanation is that although the length of the nanorods of sample B is longest, the average diameter is around twice as large as others, thus results in its relatively small surface area. The UV–visible spectroscopy results also consistent with the FE-TEM results.

To study the performance of our DSSCs based on the Al-doped ZnO nanorod arrays, the photovoltaic properties were measured under light illumination (light intensity: 200 mW/m^2, illuminance: 120,000 Lux) from a Xenon lamp. The performance characteristics were characterized after the 2 h ZnO nanorod array growth process. Fig. 7 shows the current–voltage (*J*–*V*) characteristics of the ZnO nanorod array DSSCs. The corresponding measurement results are located in Table 1. It should be noted that the principle purpose of this study is to investigate and clarify the effects of Al-doping and even higher efficiencies can be attained by increasing the length of the ZnO nanorod array. Law et al. extended ZnO nanorod length to approximately 17 μm and attained an efficiency of 1.5% [11]. The

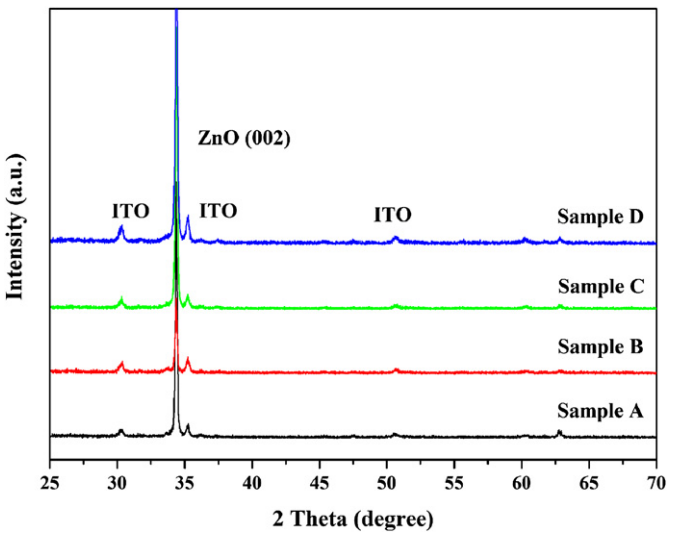

Fig. 4. XRD patterns of the Al-doped ZnO nanorod arrays on the ITO glass substrate.

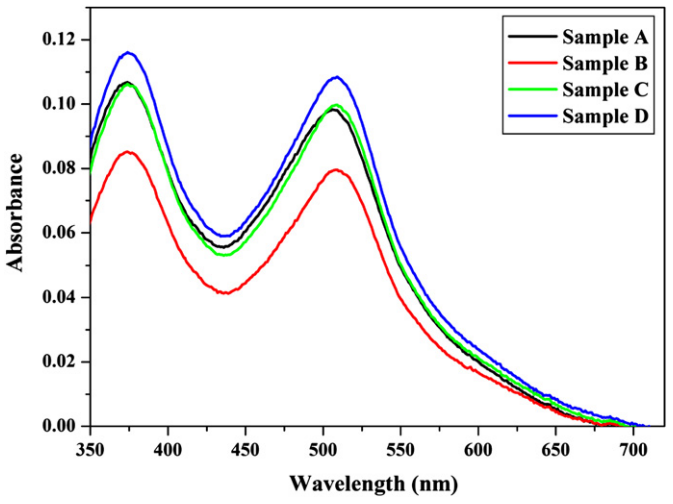

Fig. 6. UV–visible absorption spectra of the samples containing N719 dye sensitizers desorbed from the Al-doped ZnO nanorod arrays.

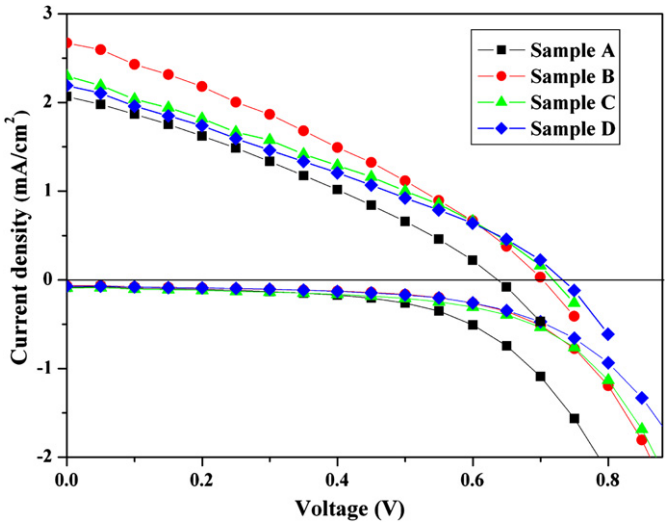

Fig. 7. *J–V* and dark *J–V* characteristic curves of the Al-doped ZnO nanorod array DSSCs, measured under light illumination (light intensity: 200 mW cm^{-2}, illuminance: 120,000 Lux).

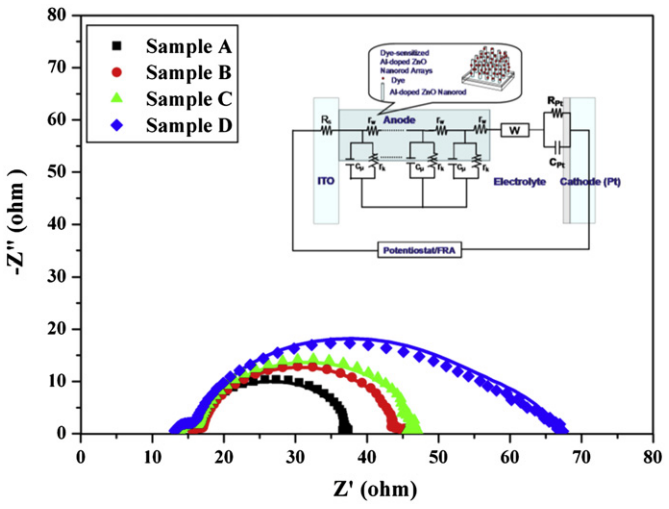

Fig. 8. Nyquist plots of the impedance data of the Al-doped ZnO nanorod array DSSCs. Inset: equivalent circuit model of the DSSCs. The solid lines are derived from the equivalent circuit model in the inset figure.

DSSC based on sample B exhibits the highest conversion efficiency and short-circuit current density (J_{sc}), even though it contains the lowest dye loading, among the prepared samples. The dark *J–V* characteristic curves of DSSCs are also shown in Fig. 7. It is universally known that the dark current in DSSC is primarily caused by the recombination of electrons at the semiconductor electrode and electrolyte interface. The results indicate that Al-doping suppresses the dark current leading to a reduction in the recombination of electrons at the interface, which results in increased V_{oc}. Plausible explanations for the V_{oc} enhancement are as follows. Al-doping in ZnO is typical *n*-type doping, which leads to an increase in charge carrier density. The electrons can partially fill the surface traps and this shifts the Fermi level toward the conduction band edge, resulting in the reduction of electron recombination at the interface [21,22]. In order to study the electrochemical properties, electrochemical impedance spectroscopy (EIS) was performed. Fig. 8 (inset) illustrates an equivalent circuit in DSSCs, derived from the diffusion-recombination model suggested by Bisquert [23,24]. This model is commonly used to investigate the electron transport properties in the DSSCs [23–25]. In the equivalent circuit model, R_s represents the lumped series resistance for the transport resistance in ITO and all the corresponding resistances outside of the cell; r_w is the specific electron transport resistance in the ZnO nanorod arrays; r_k is the specific charge-transfer resistance related to the recombination of electrons at the ZnO nanorod array electrode/electrolyte interface; c_k is the chemical capacitance of the ZnO nanorod array electrodes; *W* represents the impedance of the I_3^- diffusion in the electrolyte; R_{Pt} and C_{Pt} respectively refer to the charge-transfer resistance and interfacial capacitance at the Pt counter electrode/electrolyte interface. Fig. 8 also shows the Nyquist plots of both the measured impedance data points and the derived curves for the Al-doped ZnO nanorod array DSSCs, which were obtained under illumination and at V_{oc} conditions over the frequency range of 10^{-1} Hz to 10^5 Hz. Three arcs can be distinguished from the Nyquist plot. The arcs from left to right correspond to the frequency regions 10^3–10^5, 1–10^3, and 10^{-1}–1 Hz are assigned the impedance which is interrelated with the charge-transfer process at the Pt counter electrode, at the ZnO nanorod arrays/dye/electrolyte, and the Nernstian diffusion of redox species in the electrolyte, respectively [26]. The determination of parameters for the electron transport in the ZnO nanorod array DSSCs was done by fitting the Nyquist plots, according to the method proposed by Adachi et al. [27]. The parameters obtained by this method (r_w, r_k, k_{eff} and D_{eff}) are listed in Table 2. The value k_{eff} is the effective rate constant for the charge recombination, estimated from the peak frequency of the central arc. The value D_{eff} is the effective diffusion coefficient, which can be determined from the equation.

$$D_{eff} = (r_k/r_w)^* K_{eff}$$

Table 2
Electron transport properties of the un-doped and Al-doped ZnO nanorod array DSSCs, measured under light illumination (light intensity: 200 mW cm^{-2}, illuminance: 120,000 Lux).

Sample, % Al-doping	Thickness/ length (μm)	r_w (ohm μm^{-1})	r_k (ohm*μm)	k_{eff} (s^{-1})	D_{eff} ($\times 10^{-5}$ cm^2 s^{-1})
A, 0	2.9	0.914	62.4	70.8	4.83
B, 0.5	3.1	0.113	83.5	65.2	48.2
C, 2.5	2.7	1.08	84.2	38.9	3.03
D, 5.0	2.4	1.11	89.6	38.8	3.13

Table 1
Cell performance characteristics of the un-doped and Al-doped ZnO nanorod array DSSCs, measured under light illumination (light intensity: 200 mW cm^{-2}, illuminance: 120,000 Lux).

Sample,% Al-doping	Thickness/length (μm)	V_{oc} (V)		J_{sc} (mA cm^{-2})		FF (%)	η (%)	
A, 0	2.9	0.636	% increase	2.07	% increase	31.2	0.205	% increase
B, 0.5	3.1	0.703	10.5	2.67	29.0	31.7	0.298	45.4
C, 2.5	2.7	0.718	12.9	2.30	11.1	31.6	0.261	27.3
D, 5.0	2.4	0.732	15.1	2.12	2.4	31.0	0.241	17.6

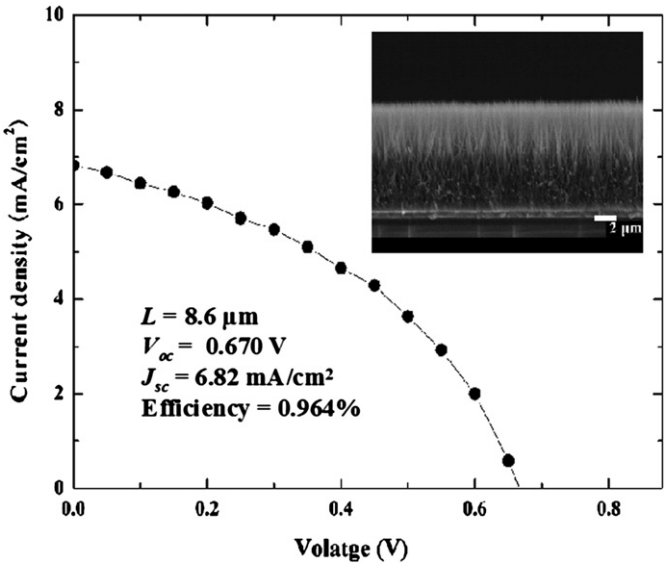

Fig. 9. *J–V* characteristic curves of DSSCs based on the Al-doped ZnO nanorod arrays of 0.5% Al content with 6 h of cumulative growth times.

As shown in Table 2, the specific electron transport resistance (r_w) in the ZnO nanorod arrays of sample B is the lowest among the samples. Al-doping in ZnO corresponds to typical *n*-type doping, which results in an increase of charge carrier density, and a decrease in resistivity. This trend is true for sample B but r_w appears to increase in sample C, D. We propose that the morphological and structural change induced by Al-doping play a pivotal role in the electron transport. As discussed previously, the morphology and structure of ZnO nanorods vary as a function of the Al content and the ZnO nanorod arrays of sample B exhibit the largest diameter, a value which is almost twice as large as other samples. The appropriate increase in the nanorod diameter is considered favorable due to a reduction in electron transport resistance, which further speeds up electron transport in the ZnO nanorod arrays. The specific electron transport resistance (r_w) in the Al-doped ZnO nanorod arrays has an upward trend with higher levels of Al-doping above 0.5%. The reason for this is due to a possible decrease in diameter or by the superfluous Al. The excess aluminum may not necessarily contribute to an increase in the charge carrier density and may result in an increase in the resistivity. With respect to the other values, the value r_k has a tendency to increase and the value k_{eff} has a tendency to decrease as a function of the Al content in the sample A, B, C and D. Such an increase in the charge recombination resistance, namely, the decrease of the charge recombination rate is consistent with the result of the dark current analysis. This result also supports the V_{oc} enhancement in the DSSCs. According to the variation of values of r_w, r_k and k_{eff}, the value of D_{eff} initially has an upward trend followed by a downward trend with higher levels of Al content. Moreover, the ZnO nanorod arrays of sample B demonstrate the highest value of D_{eff}. This reveals that the electron transport in sample B is the most effective among the samples tested. 0.5% Al-doped ZnO nanorod array DSSCs contain the lowest electron transport resistance and the highest value of effective diffusion coefficient and these are plausible reasons for the highest short-circuit current density (J_{sc}) in comparison with the other samples tested under equal conditions.

4. Conclusions

Al-doped ZnO nanorod arrays were prepared and their structure, morphology, and electrochemical properties were studied. Al-doping results in a higher overall performance in comparison with DSSCs containing un-doped ZnO nanorod arrays. The significant increase in the open-circuit voltage with the addition of Al can be attributed to the increase in electron recombination resistance at the ZnO nanorod array electrode/electrolyte interfaces resulting in the reduction in dark current. The diameter of the ZnO nanorods also changed with the addition of Al. The experimental results indicate that an appropriate increase in the diameter of one-dimensional nanostructures used as photoanode materials for DSSCs is beneficial to solar cell performance due to a reduction in electron transport resistance. The DSSC based on 0.5% Al-doping exhibits the highest observed efficiency. Given this trend, we prepared ZnO nanorod arrays with 0.5% Al content but with longer growth time resulting in a longer nanorod length. When the Al-doped ZnO nanorods were grown for 6 h (Fig. 9), the length reaches approximately 8.6 µm and the conversion efficiency increases to almost 1%. Therefore, The Al-doping revealed the capability to enhance the performance of solar cells based on ZnO nanorod arrays. Furthermore, it is worth noting that in addition to Al concentration, other factors affect the diameter of ZnO nanorods including solution concentration and the presence of a cationic polyelectrolyte [11]. Higher levels of Al-doping on the ZnO nanorod array electrode with the appropriate nanorod diameter and surface area will lead to higher performance. Therefore, it is worth investigating the limiting factor that determines the diameter of the doped ZnO nanorods so that the appropriate quantities can be optimized leading to greater overall performance.

Acknowledgments

The research is partly funded by Japan Science and Technology Agency. The authors would like to thank associate professor Yoshitaka Kitamoto from the Department of Innovative and Engineered Materials, Tokyo Institute of Technology and associate professor Manabu Ihara from the Department of Chemistry, Tokyo Institute of Technology for providing some of the necessary laboratory equipment and analysis software. The authors would also like to thank the National University Corporation Tokyo Institute of Technology Center for Advanced Materials Analysis, for FE-TEM analysis and the Center for Advanced Materials Analysis (Suzukakedai), Technical Department, Tokyo Institute of Technology, for SEM analysis.

References

[1] B. O'Regan, M. Grätzel, Nature 353 (1991) 737–740.
[2] M. Gratzel, Nature 414 (2001) 338–344.
[3] V.M. Guerin, C. Magne, T. Pauporte, T. Le Bahers, J. Rathousky, ACS Appl Mater Interfaces 2 (2010) 3677–3685.
[4] K. Sayama, H. Sugihara, H. Arakawa, Chem Mater 10 (1998) 3825–3832.
[5] V. Thavasi, V. Renugopalakrishnan, R. Jose, S. Ramakrishna, Mater Sci Eng R 63 (2009) 81–99.
[6] P. Charoensirithavorn, Y. Ogomi, T. Sagawa, S. Hayase, S. Yoshikawa, J Electrochem Soc 157 (2010) B354–B356.
[7] A.B.F. Martinson, J.W. Elam, J.T. Hupp, M.J. Pellin, Nano Lett 7 (2007) 2183–2187.
[8] D. Kuang, J. Brillet, P. Chen, M. Takata, S. Uchida, H. Miura, et al., Acs Nano 2 (2008) 1113–1116.
[9] D. Hwang, S.M. Jo, D.Y. Kim, V. Armel, D.R. MacFarlane, S.Y. Jang, ACS Appl Mater Interfaces 3 (2011) 1521–1527.
[10] J.T. Jiu, S. Isoda, F.M. Wang, M. Adachi, J Phys Chem B 110 (2006) 2087–2092.
[11] M. Law, L.E. Greene, J.C. Johnson, R. Saykally, P.D. Yang, Nat Mater 4 (2005) 455–459.
[12] S. Yodyingyong, Q. Zhang, K. Park, C.S. Dandeneau, X. Zhou, D. Triampo, et al., Appl Phys Lett 96 (2010) 073115.
[13] C.H. Ku, J.J. Wu, Nanotechnology 18 (2007) 505706.
[14] H.M. Cheng, W.H. Chiu, C.H. Lee, S.Y. Tsai, W.F. Hsieh, J Phys Chem C 112 (2008) 16359–16364.
[15] Q. Ahsanulhaq, A. Umar, Y.B. Hahn, Nanotechnology 18 (2007) 115603.

[16] P. Nunes, E. Fortunato, P. Tonello, F. Braz Fernandes, P. Vilarinho, R. Martins, Vacuum 64 (2002) 281–285.
[17] D.J. Cohen, K.C. Ruthe, S.A. Barnett, J Appl Phys 96 (2004) 459–467.
[18] S. Maniv, W.D. Westwood, E.J. Colombini, Vac Sci Technol 20 (1982) 162–170.
[19] J.G. Lu, Z.Z. Ye, Y.J. Zeng, L.P. Zhu, L. Wang, J. Yuan, et al., J Appl Phys 100 (2006) 073714.
[20] J. Zhang, W.X. Que, Sol Energy Mater Sol Cells 94 (2010) 2181–2186.
[21] X.J. Feng, K. Shankar, M. Paulose, C.A. Grimes, Angew Chem. Int Ed 48 (2009) 8095–8098.
[22] N. Ye, J.J. Qi, Z. Qi, X.M. Zhang, Y. Yang, J. Liu, et al., J Power Sources 195 (2010) 5806–5809.
[23] J. Bisquert, G. Garcia-Belmonte, F. Fabregat-Santiago, A. Compte, Electrochem Commun 1 (1999) 429–435.
[24] J. Bisquert, Phys Chem Chem Phys 2 (2000) 4185–4192.
[25] C.H. Ku, J.J. Wu, Appl Phys Lett 91 (2007) 093117.
[26] L.Y. Han, N. Koide, Y. Chiba, T. Mitate, Appl Phys Lett 84 (2004) 2433–2435.
[27] M. Adachi, M. Sakamoto, J. Jiu, Y. Ogata, S. Isoda, J Phys Chem B 110 (2006) 13872–13880.